Resonant Frequencies and Field Distributions for the Shielded Uniaxially Anisotropic Dielectric Resonator by the FD–SIC Method

Jenn-Ming Guan and Ching-Chuan Su, *Member, IEEE*

***Abstract*—New formulations for resonant modes of a shielded uniaxially anisotropic dielectric resonator (DR), such as sapphire, are proposed. They are solved by the finite-difference and simultaneous iteration with the Chebyshev (FD–SIC) acceleration method. Like an isotropic DR cavity, one azimuthal field is used for azimuthally invariant TM or TE modes and two TM fields are used for azimuthally variant hybrid modes. It is shown that the governing equation for TE modes is the same as that for the isotropic DR case. For TM and hybrid modes, more general $\psi(= rH_\phi)$ and H_r–H_z formulations than those for the isotropic DR are derived, respectively. Cylindrical cavities loaded with a rod or ring DR can be easily modeled and analyzed by the present method. Resonant frequencies and field distributions can be accurately and efficiently obtained. Numerical results of resonant frequencies of rod sapphire DR cavities are compared to those by the mode-matching method in the literature to verify the present approach. The electric- and magnetic-field distributions are also presented for hybrid modes of the uniaxially anisotropic DR cavity.**

***Index Terms*— Dielectric resonators, hybrid modes, uniaxial dielectric.**

I. Introduction

DIELECTRIC resonators (DR's) made of single-crystal materials, such as sapphire, have received considerable attention recently due to the very low-loss nature for constructing high-stability and low-noise microwave oscillators [1]–[3]. High-performance oscillators often require extremely high Q resonators fabricated of sapphire dielectric resonators shielded by high-temperature superconducting films [4]–[6]. In addition, this structure of the DR-loaded superconductor cavity is used in turn to measure the surface resistances of underdevelopment superconductors [6]–[8]. In these cases, the traditional ceramic DR's are not appropriate for these very low-loss applications. In addition to the widely used sapphire material, the other single-crystal materials to build very low-loss DR's are still under investigation [5], [9].

Resonant frequencies and field distributions of resonant modes of the isotropic DR-loaded cavity have been extensively analyzed with various methods. Basic characteristics of DR resonant modes can be found in [10] and comparisons of different numerical methods can also be found in [10] and [11]. The literature and numerical methods for analysis of the uniaxially anisotropic DR are somewhat limited compared to the isotropic DR, and are described in this paper. Approximate solutions have been used to obtain the resonant frequencies of a rod sapphire DR [12] and the field distributions of a ring sapphire DR [13]. However, the uniaxially anisotropic nature should be taken into account for accurate designs of practical applications. This demands rigorous and efficient numerical methods to analyze resonant modes of the uniaxially anisotropic DR-loaded cavity. For the kind of approaches using modal expansions, the Rayleigh–Ritz methods [14], [15] with hollow-cavity eigenfunctions as the bases and the radial mode-matching method [16] can be found. The former uses global basis functions and the latter is the commonly used mode-matching methods generalized from isotropic to anisotropic DR systems. Another kind of approach uses the discretization of fields, such as the finite-difference (FD) method or FEM. However, very few investigations can be found in the literature for the anisotropic DR. To our knowledge, only the finite-integration technique [17] with the full $\mathbf{E}$ formulation and the FEM [15] with the full $\mathbf{H}$ formulation can be found recently. The shifted power method is used to solve the resulting large matrix eigenproblem in [17]. This approach will be inefficient when a DR with somewhat large dielectric constant exists in the cavity [11], and the discretization density employed in [15] is only about 800 nodes in the r–z cross-section plane. It is preferable to use more nodes to obtain more accurate results.

In this investigation, new compact formulations for TM and hybrid modes of the uniaxially anisotropic DR cavity are proposed and derived in Section II. It is shown that the resulting governing equation of TE modes is the same as that for the isotropic DR using the azimuthal electric field. These equations and the associated boundary conditions are solved by the finite-difference and simultaneous iteration with the Chebyshev (FD–SIC) acceleration method [11]. The required central processing unit (CPU) time goes with $N^{1.5}$ and the memory space goes linearly with N, where N is the total number of unknowns [11]. As a result, accurate resonant frequencies and field distributions of the uniaxially anisotropic DR-loaded cavity can be efficiently obtained with high discretization density by the present numerical technique.

Manuscript received May 14, 1997; revised June 20, 1997. This work was supported by the National Science Council, R.O.C., under Grant NSC85-2213-E-007-001.

The authors are with the Department of Electrical Engineering, National Tsinghua University, Hsinchu, Taiwan, R.O.C.

Publisher Item Identifier S 0018-9480(97)07112-3.

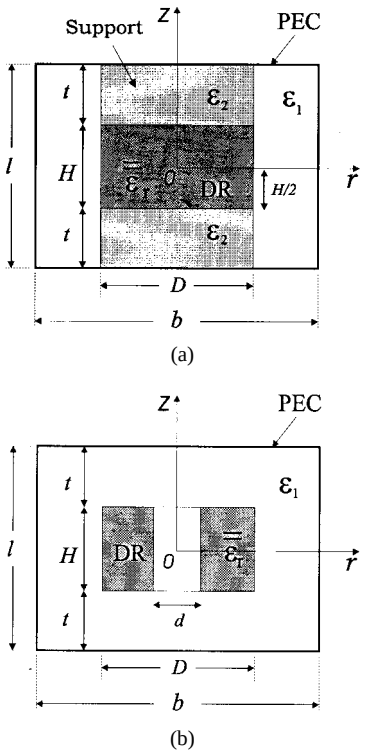

Fig. 1. Configurations of (a) uniaxially anisotropic dielectric rod resonator in the cylindrical cavity with supports and (b) uniaxially anisotropic dielectric ring resonator in the cavity.

The numerical results for the rod sapphire DR cavity are shown in Section III and are compared to those obtained with the radial mode-matching method [16]. Furthermore, the resonant electromagnetic-field distributions are presented to investigate the resonant nature of the sapphire DR cavity for some hybrid modes.

II. Formulation

The configurations of the cylindrical cavity loaded with a uniaxially anisotropic DR are shown in Fig. 1. In Fig. 1(a), a rod DR of height H and diameter D is placed between two supports with isotropic dielectric constant ϵ_2, while a ring DR of inner diameter d is placed in the cavity depicted in Fig. 1(b). Both systems are assumed to be lossless. The optical axis of the uniaxially anisotropic DR is in the z-direction. Hence, total structures with circularly cylindrical symmetry can be analyzed in the two-dimensional (2-D) r–z plane. The spatial distributions of the dielectric constant tensor in the whole cavity are given by

$$\bar{\bar{\epsilon}}(\mathbf{r}) = \bar{\bar{\epsilon}}(r, z) = \begin{bmatrix} \epsilon_r(\mathbf{r}) & 0 & 0 \\ 0 & \epsilon_r(\mathbf{r}) & 0 \\ 0 & 0 & \epsilon_z(\mathbf{r}) \end{bmatrix}. \quad (1)$$

From Maxwell's equations with nonmagnetic materials, the magnetic and electric fields satisfy the equations

$$\nabla \times [\bar{\bar{\epsilon}}^{-1}(\mathbf{r}) \cdot \nabla \times \mathbf{H}] - \omega^2 \mu_0 \epsilon_0 \mathbf{H} = 0 \quad (2a)$$

and

$$-\nabla^2 \mathbf{E} + \nabla\nabla \cdot \mathbf{E} - \bar{\bar{\epsilon}}(\mathbf{r}) k_0^2 \mathbf{E} = 0 \quad (2b)$$

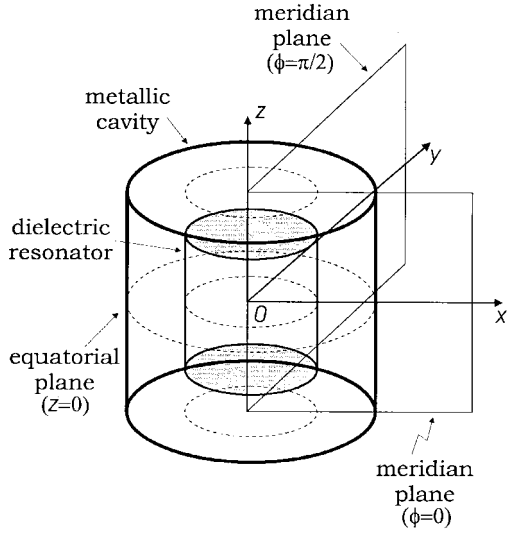

Fig. 2. 3-D view of a dielectric rod resonator in the cylindrical cavity and the equatorial and meridian planes for plots of field distributions.

respectively. To formulate the governing equations of resonant modes, it is compact and efficient to use the minimum number of field components. Furthermore, it is convenient to use the magnetic field as it is possible, since the magnetic fields are continuous across the dielectric interfaces. We show that (2a) is used for governing equations of TM and hybrid modes, and (2b) is used for TE modes. For this, several quantities in cylindrical coordinates are defined. The transverse parts (to azimuthal direction ϕ) of the vector field $\mathbf{H}$ and relative permittivity $\bar{\bar{\epsilon}}(\mathbf{r})$ are represented by $\mathbf{H}_t = \hat{r}H_r + \hat{z}H_z$ and $\bar{\bar{\epsilon}}_t = \epsilon_r \hat{r}\hat{r} + \epsilon_z \hat{z}\hat{z}$, respectively. Accordingly, the curl operator can be written as

$$\nabla \times \mathbf{H} = \nabla_t \times \mathbf{H}_t + \frac{1}{r} \nabla_t \times \hat{\phi} r H_\phi + \frac{1}{r} \hat{\phi} \times \frac{\partial}{\partial \phi} \mathbf{H}_t \quad (3)$$

where the transverse part of the ∇ operator is defined as $\nabla_t = \hat{r}(\partial/\partial r) + \hat{z}(\partial/\partial z)$.

With these definitions and notations, we can expand (2a) into its field components in cylindrical coordinates by using (3). The azimuthal and transverse components of (2a) are obtained as

$$\nabla_t \times \frac{1}{r} \left[\bar{\bar{\epsilon}}_t^{-1} \cdot \left(\nabla_t \times \hat{\phi} r H_\phi + \hat{\phi} \times \frac{\partial}{\partial \phi} \mathbf{H}_t \right) \right] - k_0^2 H_\phi = 0 \quad (4a)$$

and

$$\frac{1}{r} \nabla_t \times \left(\frac{r}{\epsilon_r} \nabla_t \times \mathbf{H}_t \right) - \frac{jm}{r^2} \hat{\phi} \times [\bar{\bar{\epsilon}}_t^{-1} \cdot (\nabla_t \times \hat{\phi} r H_\phi)] - \frac{m^2}{r^2} \hat{\phi} \times [\bar{\bar{\epsilon}}_t^{-1} \cdot (\hat{\phi} \times \mathbf{H}_t)] - k_0^2 \mathbf{H}_t = 0 \quad (4b)$$

respectively. The azimuthal dependence $e^{-jm\phi}$ is assumed for (4b). It is seen from (4a) that for the azimuthally invariant modes ($\partial/\partial\phi = 0$), the field H_ϕ is not coupled with transverse fields $\mathbf{H}_t$. Hence, we can obtain the governing equation for TM modes by using only the azimuthal field H_ϕ. For azimuthally invariant TE modes, there is no H_ϕ field. It is preferable to use the formulation with only the azimuthal electric-field E_ϕ as

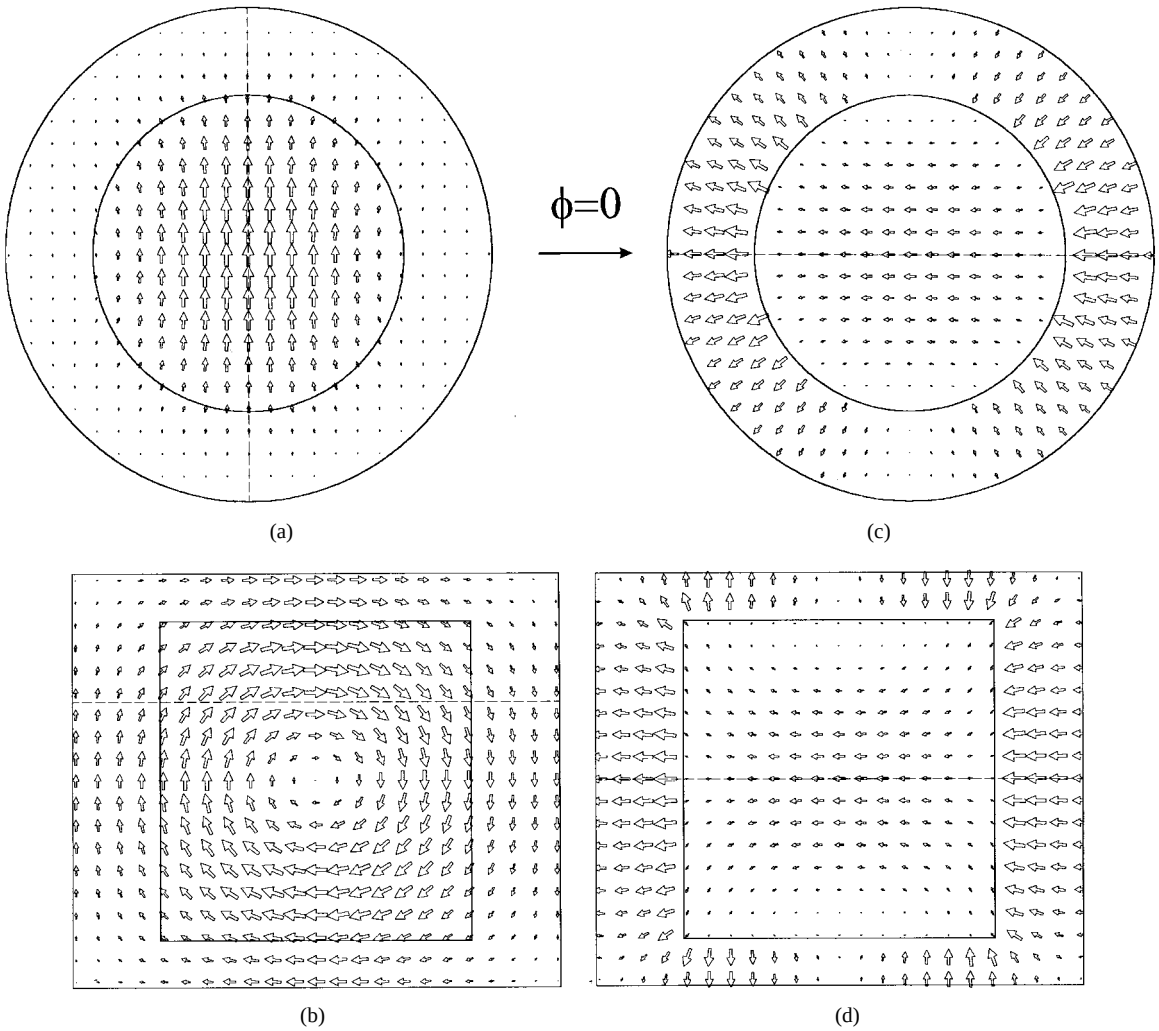

Fig. 3. Field distributions of $\mathrm{EH}_{11\delta}$ mode for the sapphire DR cavity depicted in Fig. 1(a) and considered in Case 1 of Table I. (a) Magnetic fields in the circular cross-section plane ($z = H/4$), as shown by the dashed line of (b). (b) Magnetic fields in the meridian plane $\phi = \pi/2 \cup \phi = 3\pi/2$, as shown by the dashed line of (a). (c) Electric fields in the equatorial plane, as shown by the dashed line of (d). (d) Electric fields in the meridian plane $\phi = 0 \cup \phi = \pi$, as shown by the dashed line of (c).

that for TM modes. Hence, (2b) will be used for the governing equation of TE modes. For hybrid modes ($m \neq 0$), field H_ϕ in the second term of (4b) can be uncoupled from the transverse components if it is substituted by the transverse fields $\mathbf{H}_t$ via the divergence equation of the magnetic field as

$$j\frac{m}{r}H_\phi = \frac{1}{r}\frac{\partial}{\partial r}(rH_r) + \frac{\partial H_z}{\partial z}. \tag{5}$$

Hence, only transverse fields $\mathbf{H}_t$ are used in the governing equation. The two transverse fields H_r and H_z are coupled to each other by the inhomogeneous distributions ϵ_r of the whole cavity in the first term of (4b). However, in this investigation we consider only the piecewise constant distribution of $\bar{\bar{\epsilon}}(r, z)$. At permittivity discontinuity, boundary conditions are imposed. Although H_z is not coupled to H_r at each homogeneous region, they are coupled through the boundary conditions. In the following subsections, the resulting governing equations at each homogeneous region and the required boundary conditions are presented for TM, TE, and hybrid modes, respectively.

A. TM and TE Modes

The governing equation for TM modes at each homogeneous region can be derived from (4a) as

$$\frac{\epsilon_r}{\epsilon_z}\left(\frac{\partial^2\psi}{\partial r^2} - \frac{1}{r}\frac{\partial\psi}{\partial r}\right) + \frac{\partial^2\psi}{\partial z^2} = -\epsilon_r k_0^2\psi \tag{6}$$

where $\psi = rH_\phi$. The required boundary conditions at permittivity discontinuity are the continuity of tangential electric fields. For example, for the structure depicted in Fig. 1(a), the boundary condition at uniaxially anisotropic DR interfaces is

$$\frac{1}{\epsilon_1}\frac{\partial\psi}{\partial r}\bigg|_A = \frac{1}{\epsilon_z}\frac{\partial\psi}{\partial r}\bigg|_D, \qquad \text{for interfaces parallel with } z \text{ axis} \tag{7a}$$

$$\frac{1}{\epsilon_2}\frac{\partial\psi}{\partial z}\bigg|_S = \frac{1}{\epsilon_r}\frac{\partial\psi}{\partial z}\bigg|_D, \qquad \text{for interfaces parallel with } r \text{ axis} \tag{7b}$$

where A, D, and S denote the derivatives being performed on the air, dielectric, and support sides, respectively. The

boundary conditions at the other material interfaces can be obtained similarly and the boundary conditions at the z-axis, metallic conductors, and symmetry plane are the same as those for the isotropic case [11].

For TE modes, the only nonzero field components are E_ϕ, H_r, and H_z. The divergence of electric fields is equal to zero ($\nabla \cdot \mathbf{E} = 0$) in (2b). Hence, the governing equation and boundary conditions are the same as those in isotropic mediums with scalar relative permittivity distribution $\epsilon_r(\mathbf{r})$ [11]. The governing equation is again shown as

$$\frac{\partial^2 \psi}{\partial r^2} - \frac{1}{r}\frac{\partial \psi}{\partial r} + \frac{\partial^2 \psi}{\partial z^2} = -\epsilon_r k_0^2 \psi \tag{8}$$

where $\psi = rE_\phi$. These can be expected directly because the TE modes have no E_z component, and hence, ϵ_z has no effects.

B. Hybrid Modes

For azimuthally variant modes, all six electric and magnetic fields are not zero in general. Hence, these modes are called hybrid modes. The governing equation at each homogeneous region can be presented after a little tedious, but straightforward, manipulation from (4b) and (5) as

$$\frac{\epsilon_r}{\epsilon_z}\left[\left(\frac{\partial^2}{\partial r^2} + \frac{3}{r}\frac{\partial}{\partial r} + \frac{1-m^2}{r^2}\right)H_r + \frac{2}{r}\frac{\partial H_z}{\partial z}\right] + \frac{\partial^2 H_r}{\partial z^2} - \left(1 - \frac{\epsilon_r}{\epsilon_z}\right)\frac{\partial^2 H_z}{\partial r\,\partial z} = -\epsilon_r k_0^2 H_r \tag{9a}$$

$$\left(\frac{\partial^2}{\partial r^2} + \frac{1}{r}\frac{\partial}{\partial r} - \frac{m^2}{r^2} + \frac{\partial^2}{\partial z^2}\right)H_z = -\epsilon_r k_0^2 H_z. \tag{9b}$$

This is the H_r–H_z formulation for the uniaxially anisotropic DR cavity. Compared to the formulation for isotropic mediums with scalar relative permittivity distribution $\epsilon_r(\mathbf{r})$ [11, eq. (8a), (8b)], (9b) is the same as (8b) in [11] and (9a) reduces to (8a) in [11], where $\epsilon_z = \epsilon_r$ and the term associated with $\partial^2 H_z/\partial r \partial z$ vanishes. The required boundary conditions at DR interfaces are the continuity conditions of H_ϕ and E_ϕ by the divergence (5) and the curl equation of the magnetic field, respectively. Therefore, the required boundary conditions at the material interfaces, z-axis, metallic conductors, and the symmetry plane are all the same as those in the isotropic DR cavity [11].

The associated governing equations and boundary conditions for TM, TE, and hybrid modes are solved by the newly developed FD–SIC method, which is an efficient way to solve the rendering large and sparse matrix eigenvalue problem $\mathbf{Ax} = \lambda \mathbf{x}$ [11]. Therefore, very accurate results can be obtained by using a large number of discretization points. Equally spaced meshes are preferred over graded meshes both for the simpler FD formulations and for saving the computation time and memory space. In this investigation, we use only the equally spaced node points.

III. Numerical Results

A. Comparison of Resonant Frequencies

The sapphire DR cavity with supports as depicted in Fig. 1(a) is first analyzed by using the examples used in [16]. Two different heights of DR's in the same cavity are investigated. The structure dimensions and dielectric constants are shown in Cases 1 and 2 of Table I. Equally spaced node points of 78 by 65 for the FD grid are used by using symmetry in the z-direction. Hence, there are two symmetry types for each of the TM, TE, and hybrid modes. For convenience, the mode designation shown in Table I is the same as that in [16]. EH modes are obtained by using the perfect magnetic-conductor (PMC) condition in the middle-section plane of the DR cavity, while HE modes are obtained by using the perfect electric-conductor (PEC) condition. The calculated resonant frequencies of some modes are presented in Table I. These six modes are the first mode in each group of mode type. The required computation time for one hybrid mode is about 30 s on a Pentium-166 PC. The results investigated in [16] by the mode-matching method are also shown for comparison with almost the same physical dimensions. The dimension deviations of the two investigations for DR's in two cases are within 0.15%. The maximum deviation is 0.32%, which happens at the cavity diameter b. It is seen that these two results are in good agreement and discrepancies between these two methods are within 0.4%.

TABLE I
Comparison of the Resonant Frequencies (GHz) for the Sapphire DR Cavities Depicted in Fig. 1(a) ($D = 10.0$ mm, $b = 15.6$ mm, $l = 13.0$ mm, $\epsilon_1 = 1$, $\epsilon_2 = 1.031$)

Case (1) : $H = 10.0$ mm, $\epsilon_r = 9.389$, $\epsilon_z = 11.478$

Mode	$TM_{01\delta}$	$EH_{11\delta}$	$HE_{11\delta}$	$TE_{01\delta}$	$HE_{21\delta}$	$EH_{21\delta}$
Present FD-SIC	7.359	8.845	9.113	9.706	12.048	13.522
Mode-Matching [16]	7.339	8.827	9.121	9.720	—	—
Difference	0.27%	0.20%	0.09%	0.14%	—	—

Case (2) : $H = 5.0$ mm, $\epsilon_r = 9.399$, $\epsilon_z = 11.553$

Mode	$EH_{11\delta}$	$TM_{01\delta}$	$TE_{01\delta}$	$HE_{11\delta}$	$HE_{21\delta}$	$EH_{21\delta}$
Present FD-SIC	9.873	10.696	10.696	12.163	14.595	15.254
Mode-Matching [16]	9.841	10.664	10.704	12.153	—	—
Difference	0.33%	0.30%	0.07%	0.08%	—	—

B. Resonant Field Distributions

Resonant field distributions of the above rod sapphire DR cavity are also presented in this investigation by the appropriate post-processing on the eigenfields. The tangential electric or magnetic fields of hybrid modes in some cross-section planes for Case 1 of Table I are shown. The three-dimensional (3-D) view of this DR cavity is depicted in Fig. 2, and fields are plotted in circular cross-section planes and meridian planes. Due to symmetry of the structure in the z-direction, the circular cross-section plane at $z = 0$ is the symmetry plane, called the equatorial plane [10, pp. 298–299]. The field distributions of $EH_{11\delta}$, $HE_{11\delta}$, $EH_{21\delta}$, and $HE_{21\delta}$ modes are shown in Figs. 3–6, respectively. It is known that there is a twofold

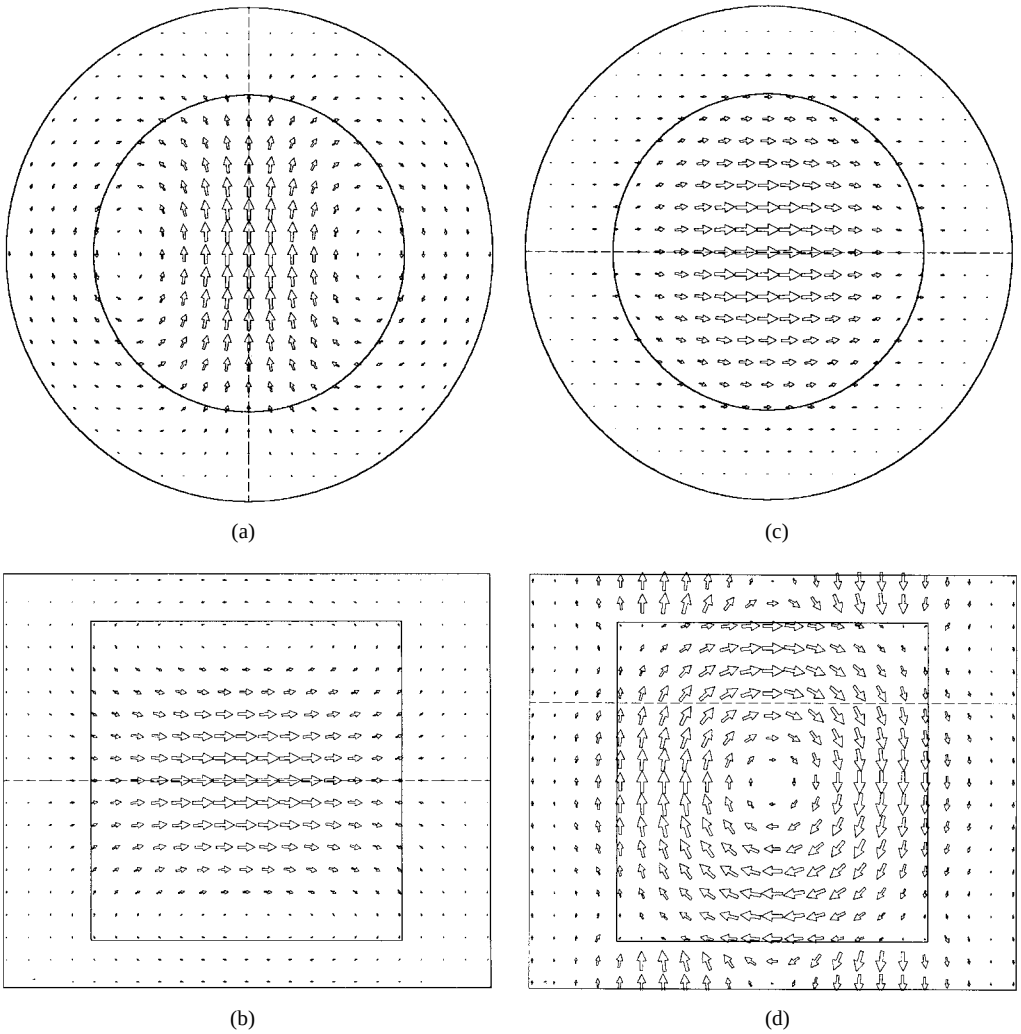

Fig. 4. Field distributions of $\mathrm{HE}_{11\delta}$ mode for the same sapphire DR cavity as Fig. 3. (a) Magnetic fields in the equatorial plane, as shown by the dashed line of (b). (b) Magnetic fields in the meridian plane, as shown by the dashed line of (a). (c) Electric fields in the circular cross-section plane ($z = H/4$), as shown by the dashed line of (d). (d) Electric fields in the meridian plane, as shown by the dashed line of (c).

degeneracy for each hybrid mode with $\cos m\phi$ and $\sin m\phi$ variations. We use $\sin m\phi$ dependence for H_r, H_z, and E_ϕ for these figures. The dependence for E_r, E_z, and H_ϕ is then $\cos m\phi$. These can be done by appropriately combining the components of $e^{jm\phi}$ and $e^{-jm\phi}$ dependence or by rewriting the formulations with $\sin m\phi$ or $\cos m\phi$ dependence. For hybrid modes, the directly available eigenfields are the TM fields H_r and H_z. The other field components can be obtained by first applying the divergence equation of the magnetic field to compute the azimuthal magnetic field H_ϕ. The electric fields are then obtained by the curl equation of the magnetic field. For the present azimuthal dependence, these field components can be written as

$$H_\phi = \frac{1}{m}\frac{\partial}{\partial r}(rH_r) + \frac{r}{m}\frac{\partial H_z}{\partial z} \tag{10a}$$

$$E_\phi = \frac{-j}{\omega\epsilon_0}\frac{1}{\epsilon_r}\left(\frac{\partial H_r}{\partial z} - \frac{\partial H_z}{\partial r}\right) \tag{10b}$$

$$E_r = \frac{-j}{\omega\epsilon_0}\frac{1}{\epsilon_r}\left(\frac{m}{r}H_z - \frac{\partial H_\phi}{\partial z}\right) \tag{10c}$$

$$E_z = \frac{-j}{\omega\epsilon_0}\frac{1}{\epsilon_z}\left[\frac{1}{r}\frac{\partial}{\partial r}(rH_\phi) - \frac{m}{r}H_r\right]. \tag{10d}$$

In Figs. 3–6, magnetic fields are shown in (a) and (b), and electric fields in (c) and (d), respectively. Eigenfield distributions, i.e., H_r and H_z fields, are shown in (b) in the meridian plane for some ϕ as indicated by the dashed line in (a). For $m = 1$ modes, such a plane is $\phi = \pi/2 \cup \phi = 3\pi/2$. For $m = 2$ modes, that is $\phi = \pi/4 \cup \phi = 5\pi/4$. This is because fields are maximum at such planes. Field plots of electric components E_r and E_z are shown in (d) in the meridian plane ($\phi = 0 \cup \phi = -\pi$) as indicated by the dashed line in (c). The magnetic- and electric-field components H_r, H_ϕ, and E_r, E_ϕ (or H_x, H_y, and E_x, E_y) in the circular cross-section plane are also shown in (a) and (c), respectively, at some constant z, as indicated by the dashed lines in (b) and (d), respectively. It is noted that the electric and magnetic fields are in time quadrature with each other. The magnetic fields lead the electric fields by $\omega t = \pi/2$ for Figs. 3–6. These field distributions are useful for establishing the coupling or exciting structures for these modes. For more clarity of field behaviors in those circular cross-section planes, the corresponding normalized field plots along the radial direction $H_r(r)$, $H_\phi(r)$, or $E_r(r)$, $E_\phi(r)$

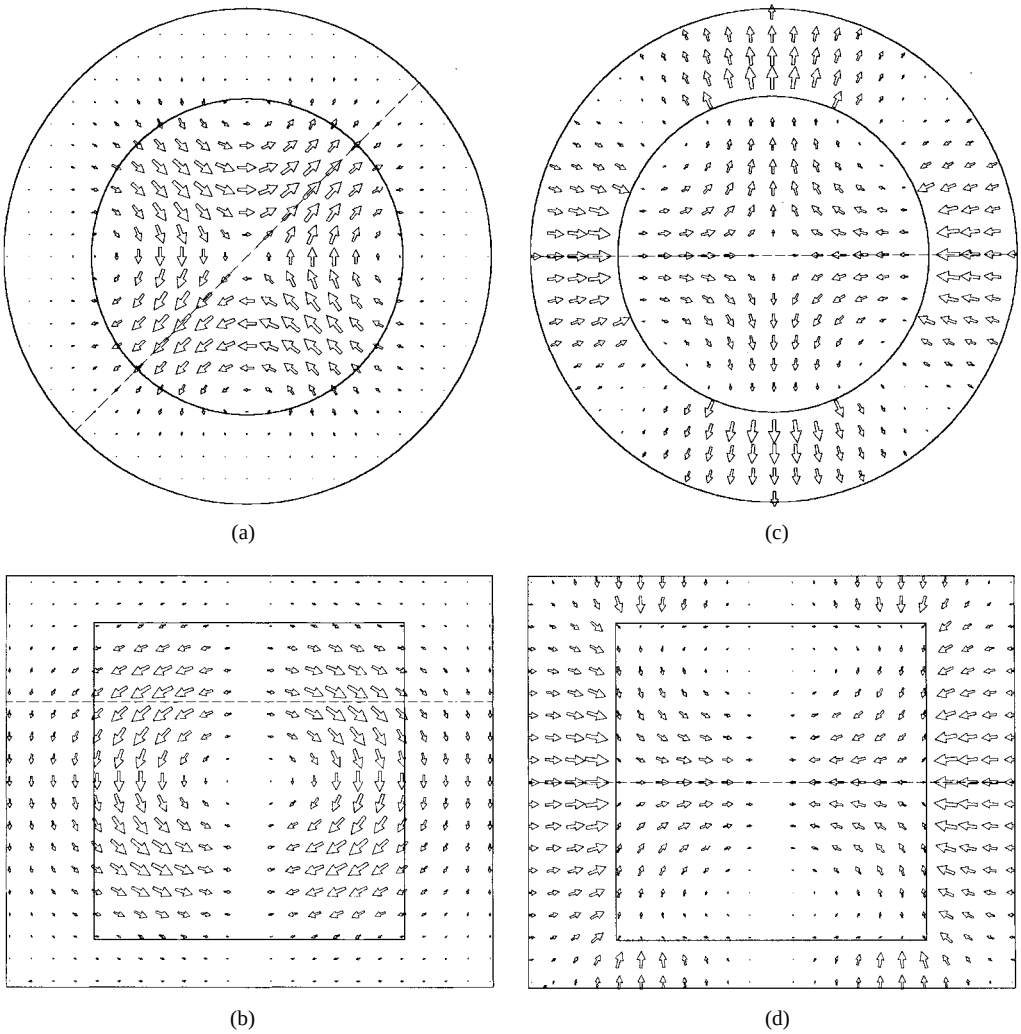

Fig. 5. Field distributions of $\mathrm{EH}_{21\delta}$ mode for the same sapphire DR cavity as Fig. 3. (a)–(b) Magnetic and (c)–(d) electric fields in the planes, as shown by the dashed lines in parts (b), (a), (d), and (c), respectively.

are shown in Figs. 7 and 8 for $m = 1$ and $m = 2$ modes, respectively.

Let us investigate the characteristics of these field distributions. The length of arrows is proportional to the magnitude of vectors within each part of these figures. Let us first take an overview of these figures. It is seen from Fig. 3 that for the $\mathrm{EH}_{11\delta}$ mode, large magnetic fields are distributed mainly in the DR but not small outside the DR, and large electric fields are located outside the DR region. On the other hand, it is seen from Fig. 4 that for the $\mathrm{HE}_{11\delta}$ mode, large magnetic fields are located in the DR region, and large electric fields are not only in the DR but also extending to the support regions. For Figs. 5 and 6, large field locations of the $\mathrm{EH}_{21\delta}$ and $\mathrm{HE}_{21\delta}$ modes are somewhat like those of the $\mathrm{EH}_{11\delta}$ and $\mathrm{HE}_{11\delta}$ modes, respectively. However, large magnetic fields of the $\mathrm{EH}_{21\delta}$ mode and large electric fields of the $\mathrm{HE}_{21\delta}$ mode are more concentrated inside the DR than the $\mathrm{EH}_{11\delta}$ and $\mathrm{HE}_{11\delta}$ modes, respectively.

The field behavior shown in Figs. 3(a), 4(a), 5(a) and 6(a) is examined to show the common and different characteristics between modes. For the magnetic fields shown in Figs. 3(a) and 4(a) for $m = 1$, there are some similarities between the two plots at first glance. However, the fields of the $\mathrm{HE}_{11\delta}$ mode form curled loops, but those of the $\mathrm{EH}_{11\delta}$ mode do not. This can be confirmed by the plot in the upper part of Fig. 7 that H_ϕ of the $\mathrm{HE}_{11\delta}$ mode goes to negative before the DR interface position as r increases. While, H_ϕ of the $\mathrm{EH}_{11\delta}$ mode remains positive toward the metallic boundary. Thus, the $\mathrm{EH}_{11\delta}$ fields do not turn around. For the magnetic fields shown in Figs. 5(a) and 6(a) for $m = 2$, these two fields are very similar to each other, as also seen from the upper part of Fig. 8. It is noted from Figs. 7 and 8 that the first derivative of $H_\phi(r)$ is discontinuous at the DR interface position, which can be verified by (10d). For the electric fields shown in (c) and (d) of Figs. 3–6, the normal components will become large near the outside of the DR interfaces if they are not too small near the inside of the DR interfaces. This is due to the continuity of the normal components of electric displacement vectors $\mathbf{D} = \epsilon_0 \bar{\bar{\epsilon}} \mathbf{E}$, and the permittivity difference between the two mediums is about one order of magnitude. Thus, $E_r(r)$ is not continuous at $r = 5$ mm, as shown in the lower parts of Figs. 7 and 8. For the EH modes in the circular planes of (c), most $\mathbf{E}$ fields are almost normal to the DR circumference, and in the meridian planes of (d), most $\mathbf{E}$ fields near the inside of the DR

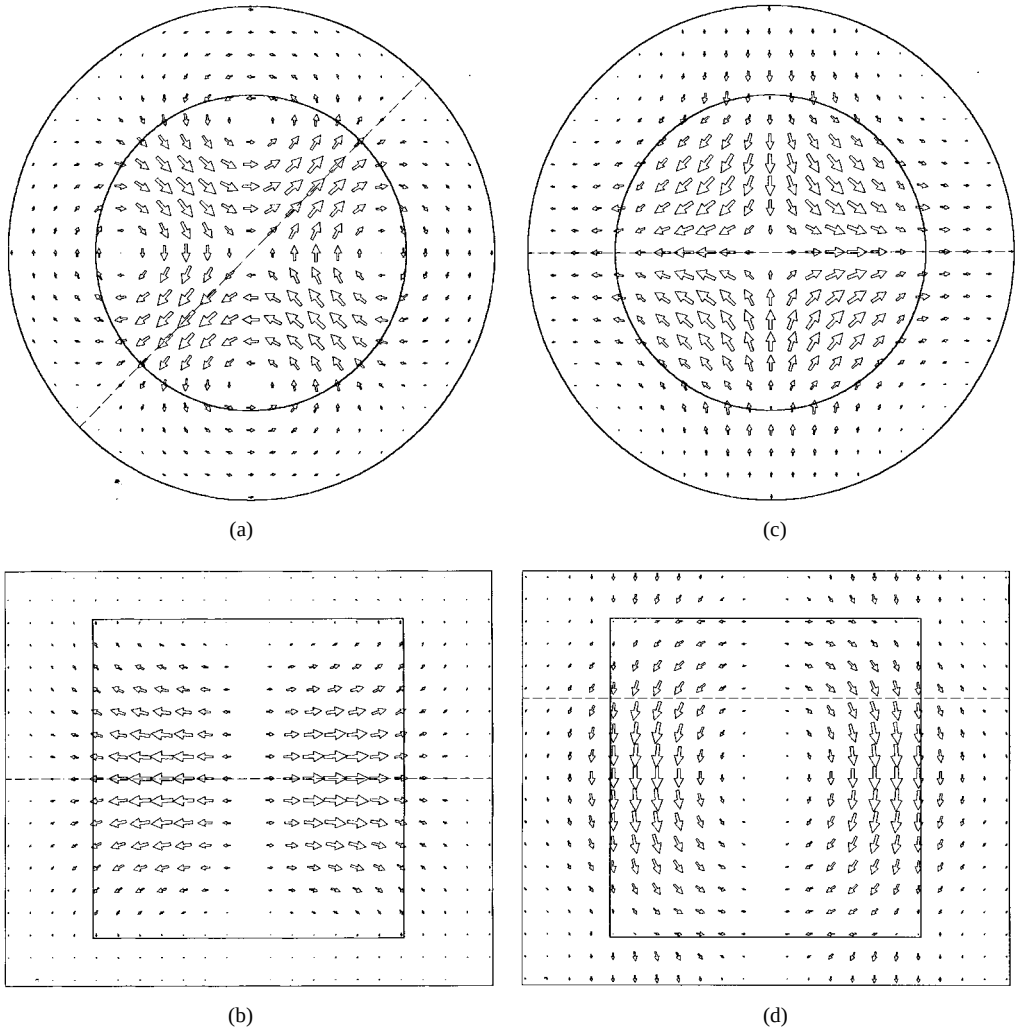

Fig. 6. Field distributions of $\mathrm{HE}_{21\delta}$ mode for the same sapphire DR cavity as Fig. 3. (a)–(b) Magnetic and (c)–(d) electric fields in the planes, as shown by the dashed lines in parts (b), (a), (d), and (c), respectively.

interface are not nearly tangential to the DR periphery. Thus, near the outside of the DR interface, most $\mathbf{E}$ fields increase and are almost normal to the DR circumference or periphery. These large $\mathbf{E}$ fields extend normally to the metallic enclosure which are not away from the DR interface. Hence, large $\mathbf{E}$ fields are maintained outside the DR region. On the other hand, for the HE modes, it seemed that most $\mathbf{E}$ fields are tangential to the DR circumference or periphery in (c) and (d). Thus, most fields do not increase in magnitude outside the DR region except for the $\mathrm{HE}_{11\delta}$ mode in the support region. Hence, large $\mathbf{E}$ fields are maintained in the DR region.

Present field distributions with the aspect ratio $H/D = 1$ are compared to those of the open isotropic DR with $H/D = 0.44$ presented in [10] or [18, pp. 307–316]. It can be seen that field patterns of the $\mathrm{HE}_{11\delta}$ and $\mathrm{HE}_{21\delta}$ modes are similar to those of the corresponding $\mathrm{HEM}_{11\delta}$ and $\mathrm{HEM}_{21\delta}$ modes in [18], even though the aspect ratios differ much. Since magnetic and electric fields are mainly concentrated in the DR, the metallic enclosure does not have much effect on these two modes. More clearly, the $\mathrm{HE}_{21\delta}$ mode is more like the corresponding mode and less affected by the enclosure than the $\mathrm{HE}_{11\delta}$ mode, for which in the support regions, electric fields with large normal components to DR interfaces still exist. On the other hand, the $\mathrm{EH}_{11\delta}$ mode is much deviated from the corresponding $\mathrm{HEM}_{12\delta}$ mode in [18]. Since there are no enclosure cavity in [18], all the resonant modes belong to DR-type or interior modes [10, p. 191] in which the major electromagnetic fields are located in or near the DR region. For the present $\mathrm{EH}_{11\delta}$ mode, large electric fields fill between the DR and enclosure for the reasons stated in the preceding paragraph. Hence, the metallic enclosure has a large effect on the $\mathrm{EH}_{11\delta}$ mode to change the field patterns of the original associated DR-type mode. The fields of $\mathrm{HEM}_{22\delta}$ mode are not shown in [10] and [18]. Based on the same reason as the $\mathrm{EH}_{11\delta}$ mode, the $\mathrm{EH}_{21\delta}$ mode can be expected to be much affected by the enclosure from the electric-field distributions. Therefore, the $\mathbf{E}$ field orientations inside the DR region have much influence on whether this mode is affected by the metallic enclosure. The $\mathrm{EH}_{11\delta}$ and $\mathrm{EH}_{21\delta}$ modes are like the mixed-type modes, while the $\mathrm{HE}_{11\delta}$ and $\mathrm{HE}_{21\delta}$ modes are like the DR-type modes [10, p. 191].

C. Parameter Analysis

The present numerical method can also analyze the cylindrical cavity loaded with a uniaxially anisotropic dielectric ring

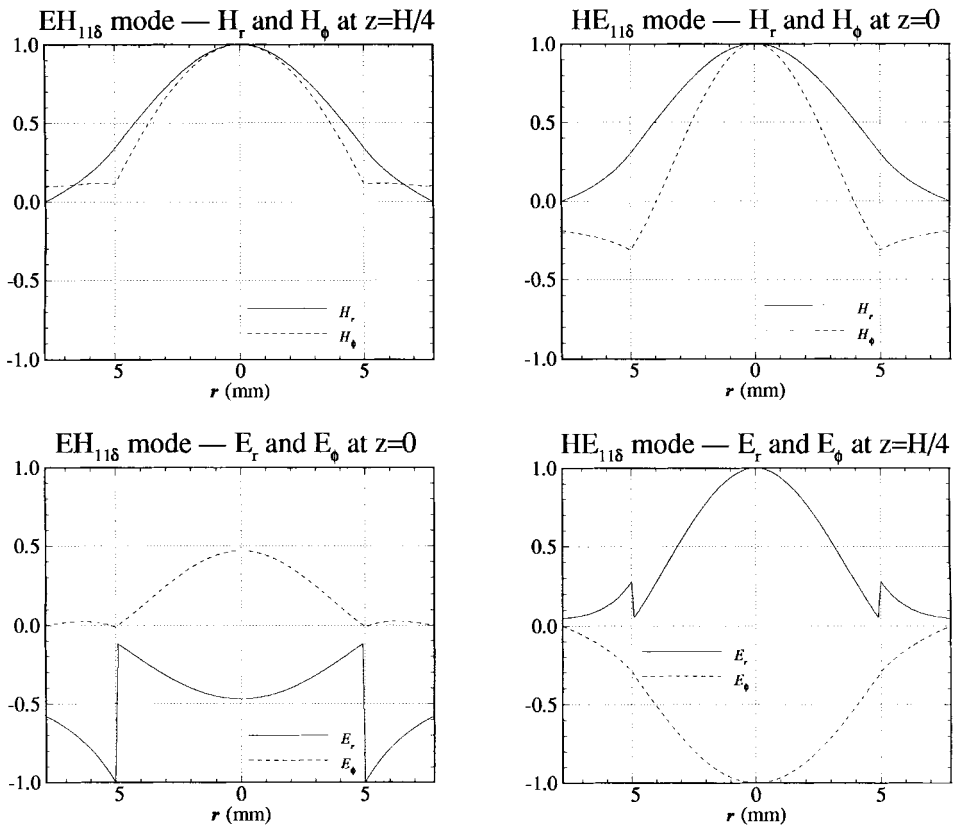

Fig. 7. Normalized field plots of $H_r(r)$, $H_\phi(r)$, $E_r(r)$, and $E_\phi(r)$ for $\mathrm{EH}_{11\delta}$ and $\mathrm{HE}_{11\delta}$ modes corresponding to Figs. 3 and 4.

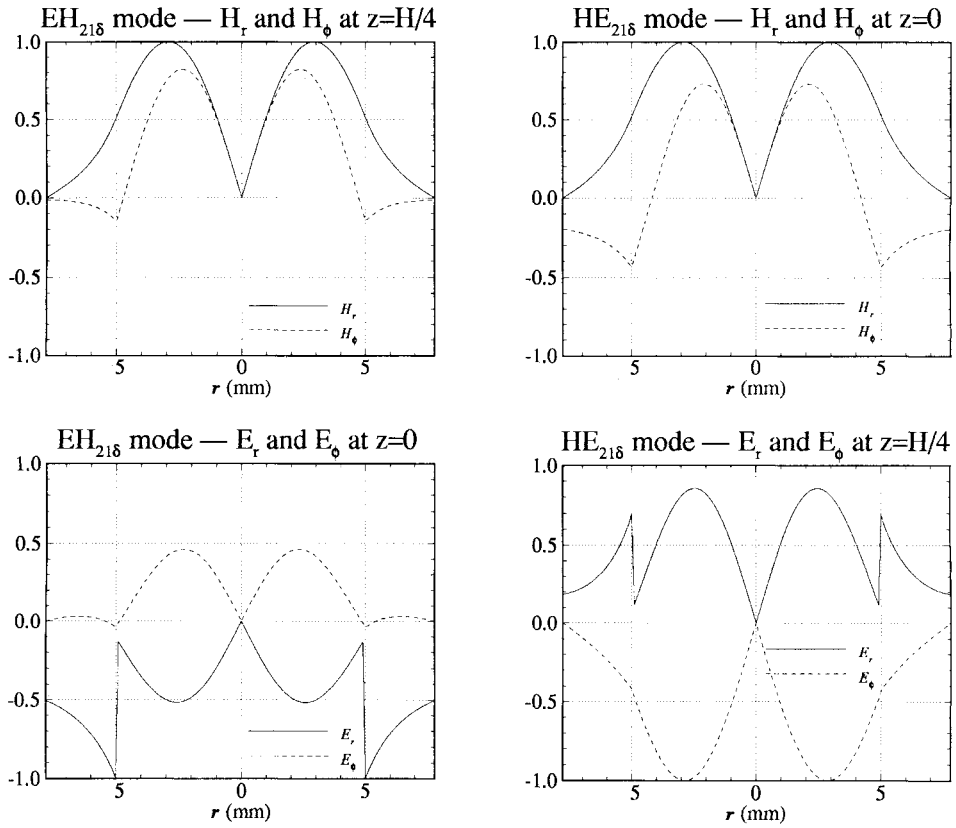

Fig. 8. Normalized field plots of $H_r(r)$, $H_\phi(r)$, $E_r(r)$, and $E_\phi(r)$ for $\mathrm{EH}_{21\delta}$ and $\mathrm{HE}_{21\delta}$ modes corresponding to Figs. 5 and 6.

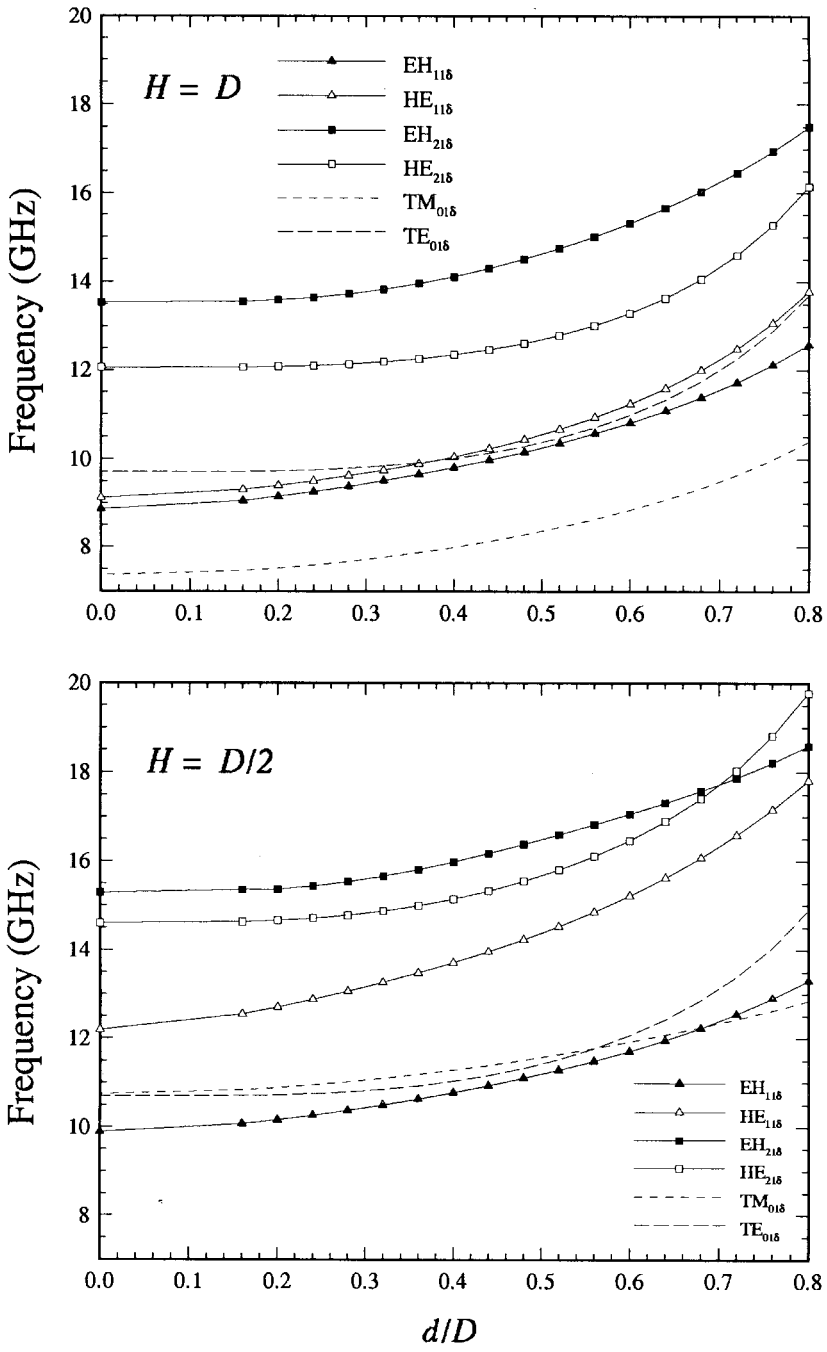

Fig. 9. Resonant frequency variations for the two cases in Table I as functions of the inner-to-outer diameter ratio d/D. Case 1: $H = D$. Case 2: $H = D/2$].

resonator without more complexity in formulations. Hence, we will show the resonant frequency variations, if the two rod sapphire DR cavities discussed in Table I are replaced by rings with an inner diameter d. For simplicity, supports are not included, as shown in Fig. 1(b), in the following parameter analyses. It can be expected that the influences of supports are very small, as the dielectric constant of supports is very close to that of the air. Resonant frequency variations for two DR's discussed in Table I are shown in Fig. 9 as functions of the inner-to-outer diameter ratio d/D. Height H is equal to diameter D for Case 1, and H is equal to one half of D for Case 2. We also perform the parameter study of height H for the rod DR in Case 1 and for the ring DR with $d/D = 0.5$. The results are shown in Fig. 10. These mode charts are useful for designing the DR cavity and for parameter optimization of operating modes. It is seen from Fig. 9 that the $\mathrm{TM}_{01\delta}$ mode is fundamental when $H = D$ and separations from the other modes are rather large in the whole d/D range. The $\mathrm{EH}_{11\delta}$ mode is fundamental when $H = D/2$ and the resonant frequency will be close to those of $\mathrm{TM}_{01\delta}$ and $\mathrm{TE}_{01\delta}$ modes as d increases. Where the fundamental mode is can be determined by the H for the present DR cavity. It is seen from Fig. 10 that the $\mathrm{TM}_{01\delta}$ mode is fundamental when the ratio H/D is larger than about 0.7 and 0.6 for the rod and ring DR cavities, respectively. While, the $\mathrm{EH}_{11\delta}$ mode is fundamental when H is smaller. In addition, resonant frequencies of $\mathrm{EH}_{11\delta}$, $\mathrm{EH}_{21\delta}$,

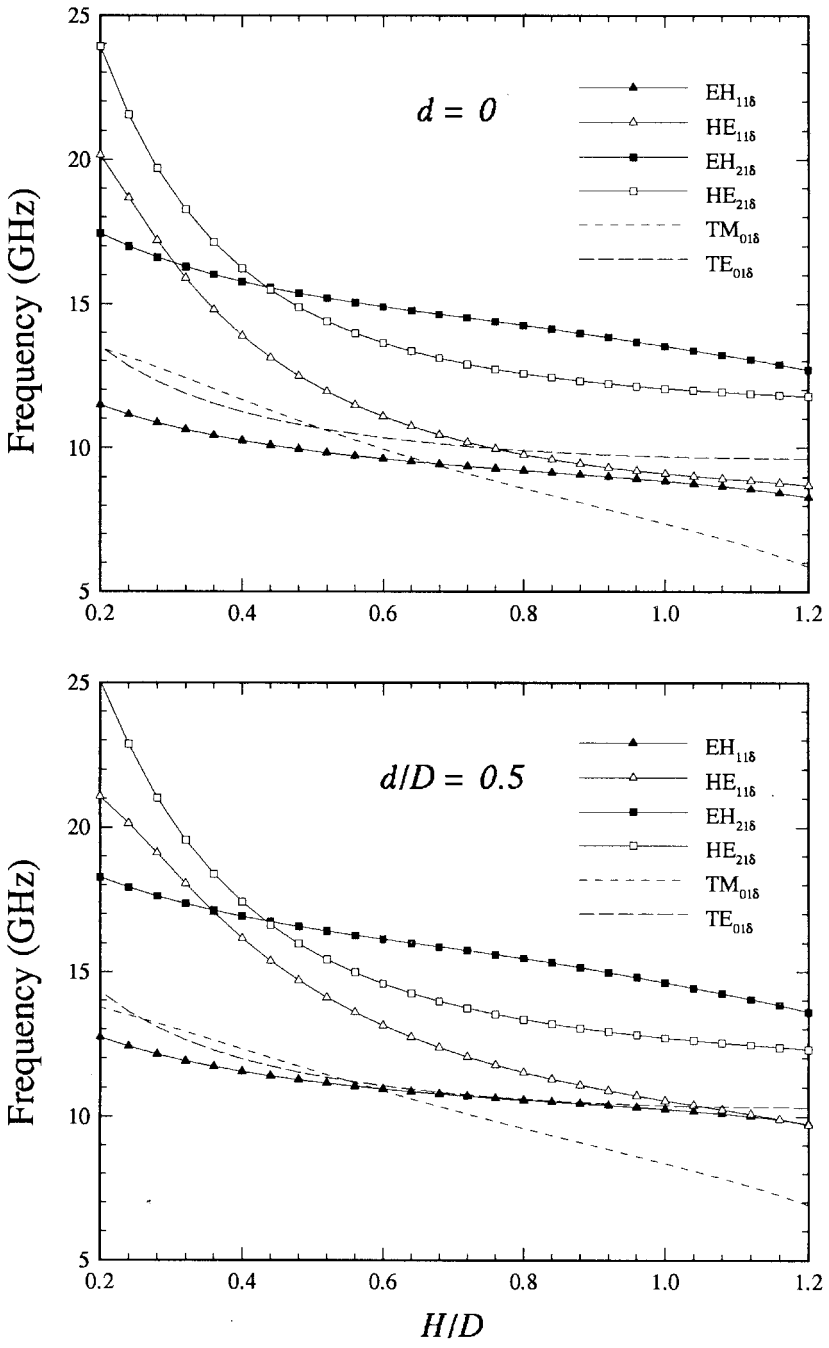

Fig. 10. Resonant frequency variations for the rod DR cavity ($d = 0$) and the ring DR cavity ($d/D = 0.5$) as functions of the height-to-outer-diameter ratio H/D.

and $\mathrm{TE}_{01\delta}$ modes vary less for the whole H/D range than those of $\mathrm{HE}_{11\delta}$, $\mathrm{HE}_{21\delta}$, and $\mathrm{TM}_{11\delta}$ modes do.

IV. Conclusion

The associated governing equations and boundary conditions for resonant modes of the cavity loaded with a uniaxially anisotropic DR have been rigorously analyzed and efficiently solved by the FD–SIC method. For TM and hybrid modes, new formulations are presented in compact form. The numerical results of resonant frequencies are close to those with the mode-matching method. In addition, field distributions of the hybrid modes are provided to investigate the characteristics of resonant modes. These field plots are also compared to the renowned plots for the open isotropic DR. Due to the versatile ability of the FD method, DR-loaded cavities with the tuning element can be easily modeled. Therefore, the FD–SIC method is very convenient in designing the sapphire or the other single-crystal DR-loaded cavity resonators.

References

[1] G. J. Dick and J. Saunders, "Measurement and analysis of a microwave oscillator stabilized by a sapphire dielectric ring resonator for ultra-low noise," *IEEE Trans. Ultrason. Ferroelect. Freq. Contr.*, vol. 37, pp. 339–346, Sept. 1990.

[2] A. J. Giles, S. K. Jones, D. G. Blair, and M. J. Buckingham, "A very high stability sapphire loaded superconducting cavity oscillator," *Physics B*, vol. 165, pp. 145–146, 1990.
[3] M. E. Tobar, E. N. Ivanov, R. A. Woode, J. H. Searls, and A. G. Mann, "Low noise 9-GHz sapphire resonator-oscillator with thermoelectric temperature stabilization at 300 Kelvin," *IEEE Microwave Guided Wave Lett.*, vol. 5, pp. 108–110, Apr. 1995.
[4] Z. Y. Shen, C. Wilker, P. Pang, W. L. Holstein, D. W. Face, and D. J. Kountz, "High T_c superconductor-sapphire microwave resonator with extremely high Q-values up to 90 K," *IEEE Trans. Microwave Theory Tech.*, vol. 40, pp. 2424–2432, Dec. 1992.
[5] N. Klein, A. Scholen, N. Tellmann, C. Zuccaro, and K. W. Urban, "Properties and applications of HTS-shielded dielectric resonators: A state-of-the-art report," *IEEE Trans. Microwave Theory Tech.*, vol. 44, pp. 1369–1373, July 1996.
[6] M. Manzel *et al.*, "High Q-value resonators for the SHF-region based on TBCCO films," *IEEE Trans. Microwave Theory Tech.*, vol. 44, pp. 1382–1384, July 1996.
[7] A. P. Mourachkine and A. R. F. Barel, "Microwave measurement of surface resistance by the parallel-plate dielectric resonator method," *IEEE Trans. Microwave Theory Tech.*, vol. 43, pp. 544–551, Mar. 1995.
[8] J. Krupka, M. Klinger, M. Kuhn, A. Baranyak, and M. Stiller, "Surface resistance measurements of HTS films by means of sapphire dielectric resonator technique," *IEEE Trans. Appl. Superconduct.*, vol. 3, pp. 3043–3048, 1993.
[9] J. Krupka, R. G. Geyer, M. Kuhn, and J. H. Hinken, "Dielectric properties of single crystals of Al_2O_3, $LaAlO_3$, $NdGaO_3$, $SrTiO_3$, and MgO at cryogenic temperatures," *IEEE Trans. Microwave Theory Tech.*, vol. 42, pp. 1886–1890, Oct. 1994.
[10] D. Kajfez and P. Guillon, *Dielectric Resonators.* Norwood, MA: Artech House, 1986.
[11] C. C. Su and J. M. Guan, "Finite-difference analysis of dielectric-loaded cavities using the simultaneous iteration of the power method with the Chebyshev acceleration technique," *IEEE Trans. Microwave Theory Tech.*, vol. 42, pp. 1998–2006, Oct. 1994.
[12] M. E. Tobar and A. G. Mann, "Resonant frequencies of higher order modes in cylindrical anisotropic dielectric resonators," *IEEE Trans. Microwave Theory Tech.*, vol. 39, pp. 2077–2082, Dec. 1991.
[13] D. G. Santiago, G. J. Dick, and A. Prata, Jr., "Mode control of cryogenic whispering-gallery mode sapphire dielectric-ring resonators," *IEEE Trans. Microwave Theory Tech.*, vol. 42, pp. 52–55, Jan. 1994.
[14] J. Krupka, "Resonant modes in shielded cylindrical ferrite and single-crystal dielectric resonators," *IEEE Trans. Microwave Theory Tech.*, vol. 37, pp. 691–697, Apr. 1989.
[15] J. Krupka, D. Cros, M. Aubourg, and P. Guillon, "Study of whispering gallery modes in anisotropic single-crystal dielectric resonators," *IEEE Trans. Microwave Theory Tech.*, vol. 42, pp. 56–61, Jan. 1994.
[16] Y. Kobayashi and T. Senju, "Resonant modes in shielded uniaxial-anisotropic dielectric rod resonators," *IEEE Trans. Microwave Theory Tech.*, vol. 41, pp. 2198–2205, Dec. 1993.
[17] D. Schmitt and T. Weiland, "2d and 3d computations of eigenvalue problems," *IEEE Trans. Magn.*, vol. 28, pp. 1793–1796, 1992.
[18] D. Kajfez, A. W. Glisson, and J. James, "Computed modal field distributions for isolated dielectric resonators," *IEEE Trans. Microwave Theory Tech.*, vol. MTT-32, pp. 1609–1616, Dec. 1984.

Jenn-Ming Guan was born in Taipei, Taiwan, R.O.C., on October 17, 1967. He received the B.S. degree in electrical engineering from National Tsinghua University, Hsinchu, Taiwan, in 1989, and the M.S. degree in electrical engineering from National Taiwan University, Taipei, in 1991. Since 1991, he has been working toward the Ph.D. degree at National Tsinghua University.

His research interests include the microwave components and numerical methods for the design of waveguides, DR's, and antennas.

Ching-Chuan Su (M'87) was born in Taiwan, R.O.C., on October 2, 1955. He received the B.S., M.S., and Ph.D. degrees in electrical engineering from National Taiwan University, Taipei, in 1978, 1980, and 1985, respectively.

From 1980 to 1982, he was employed at the Industrial Technology Research Institute, Hsinchu, Taiwan, where he was responsible for the development of several IC fabrication processes for MOS products. In 1985, he joined the faculty of National Tsinghua University, Hsinchu, where he is an Associate Professor of electrical engineering. His research interests include electromagnetic theory, numerical solutions in scattering, waveguide, resonator, and MOS circuits, and fabrication of ferroelectric memory IC's.